THE SOUNDS OF SEAS IN SPACE: THE 'WATERFALLS' OF TITAN AND THE ICE SEAS OF EUROPA

TG Leighton ISVR, Southampton University, Highfield, Southampton, SO17 1BJ, UK.
PR White ISVR, Southampton University, Highfield, Southampton, SO17 1BJ, UK.
DC Finfer ISVR, Southampton University, Highfield, Southampton, SO17 1BJ, UK.
EJ Grover ISVR, Southampton University, Highfield, Southampton, SO17 1BJ, UK

1 INTRODUCTION

The characteristics of acoustic sensors tally well with the constraints of space travel: acoustic instrumentation is low-cost, rugged and durable, has low power consumption, and generates signals of low bandwidth compared to the imaging systems more usually exploited off-world. This paper provides an acoustical consideration of two extraterrestrial seas, on moons of Saturn and Jupiter. Section 2 examines one aspect of the potential for the use of acoustics in off-world missions by consideration of what information might be retrieved from acoustical signals associated with the *Cassini-Huygens* mission to Titan. The investigation and first predictions were made prior to the landing of *Huygens*, and considered what information could be derived from the acoustics in two possible circumstances: if the descent had ended with a splashdown in liquid; or (perhaps less likely) if the landing site had been close to a methane-fall (Figure 1(a)). Whilst eventually *Huygens* managed to transmit for several hours on the surface, many expected only 3 minutes of battery life would remain after landing. One aspect which section 2 of this paper addresses is what information could be available were one ever to use acoustics in order to reduce the functionality of a probe, such that power is conserved sufficiently to allow a landed mission extended life. This very question would be particular germane to a future mission to Europa, as a long-life mission would allow investigation of the changing environment as the moon orbits Jupiter. Acoustics in particular may be of particular use in investigating this ice-covered ocean, a factor which is discussed in section 3.

(a)  (b) 

Figure 1. (a) An artist's impression of Titan's surface, undertaken prior to the mission landing. In the sky, Saturn is visible dimly in the background through Titan's thick atmosphere. The Cassini spacecraft flies over the surface with its High Gain Antenna pointed at the Huygens probe as it nears the end of its parachute descent. Thin methane clouds dot the horizon, and a narrow methane spring or "methanefall" flows from the cliff at left and produces considerable vapour. Smooth ice features rise out of the methane/ethane lake, and crater walls can be seen far in the distance. (Illustration by David Seal, Image credit: NASA/JPL/Caltech). (b) The Salmon Leap, Sadler's Mill, Romsey (Longitude 1º30' W; Latitude 50º 59'N). View to the South-south-west, looking downstream towards the Broadlands estate. The hydrophone was placed at a depth of 10 cm in clear water, about 3 m from the turbulent bubble cloud. (Photograph: T G Leighton).

2 TITAN

2.1 Previous acoustical studies

After a 7-year journey on NASA's *Cassini* spacecraft, the European Space Agency's *Huygens* probe landed on Saturn's largest moon, Titan, on 14 January 2005 (Figure 2). It takes a moment to understand the step-change in knowledge that took place on that day. The surface of the planet is obscured with smog, and while we could envisage the possibility of seas, waves and 'waterfalls', and the equivalent of Earth's water cycle based on liquid methane and ethane, when the investigation of this paper began, we had no sure knowledge that these existed[1-3]. *Huygens* was ingeniously designed to cope with a range of terrains, from liquid to solid, and an acoustic capability was included[4].

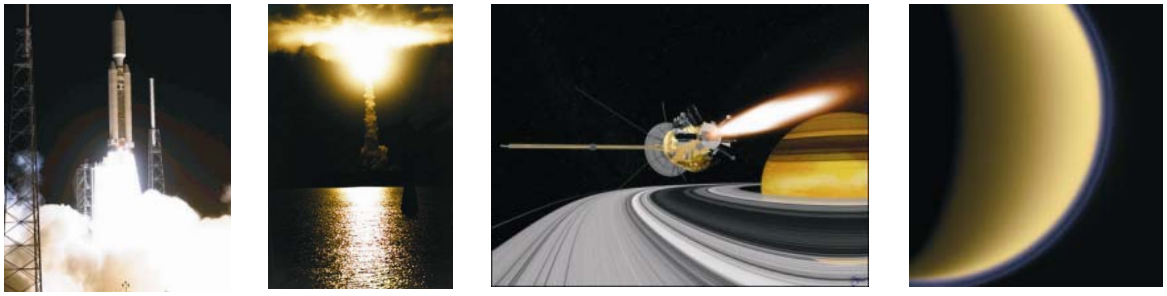

(a) (b) (c) (d)

Figure 2. (a) The start and (b) the end of the launch of the *Cassini-Huygens* spacecraft on 15 October 1997, using a Titan IV-B/Centaur launch vehicle from Florida's Cape Canaveral Air Station. (c) Throughout the night of 30 June/1 July 2004 the Cassini-Huygens spacecraft successfully completed its Saturn Orbit Insertion (SOI) manoeuvre. This is a computer-rendered image of Cassini-Huygens during the SOI manoeuvre, just after the main engine has begun firing. The spacecraft is moving out of the plane of the page and to the right (firing to reduce its spacecraft velocity with respect to Saturn) and has just crossed the ring plane. The SOI manoeuvre, which was approximately 90 minutes long, allowed Cassini to be captured by Saturn's gravity into a five-month orbit. (d) Encircled in purple stratospheric haze, Titan appears as a softly glowing sphere in this colorized image taken on July 3, 2004, one day after Cassini's first flyby of that moon. Titan has a dense atmosphere composed primarily of nitrogen with a few percent methane. The atmosphere can undergo photochemical processes to form hazes. (Image credit: NASA/JPL/Caltech).

Whilst it is recognised that acoustic technology could never replace imaging, the possibility was explored as to what could be gained were only the acoustic systems to be operational after landing: "If there is a splash and not a crunch when the probe lands, that would make Titan the first known body other than Earth to have an ocean open to an atmosphere. This would mean there could be babbling brooks and streams; and a beach at minus 180 degrees C" (quote)[5]. In the first stage[2] of the project, an appropriate model for the emission of bubbles was chosen and used to invert the sound of a terrestrial waterfall (the Salmon Leap, at Sadler's Mill, Romsey, Hampshire, UK – see Figure 1(b)). Such inversions are not uncommon. They range from the identification of individual bubble signatures with entrainments of bubbles of calculated sizes[6] (later augmented by use of the Gabor transform when entrainment rates or noise were high[7]), to the recreation of the overall power spectrum using the cumulative spectral content of naturally-emitting bubbles. The latter approach was pioneered by Loewen and Melville[8]. None of these models are entirely suitable[9] (see sections 2.2 and 2.4): the initial study[2] used a monopole version of the model of Loewen and Melville[8], although with the heuristic approach to the amplitude of the bubble pulsations replaced by a physics-based one. The Salmon Leap bubble population was then used to estimate the sound that a methane-fall would make, if there were one on Titan which had the same entrainment statistics (not an unreasonable suggestion given the fluid parameters[2]). The reconstructed power spectrum for the terrestrial waterfall agreed with the measured Salmon Leap data, allowing some credibility to be given to the predicted spectrum for Titan (although it is recognised that this is check can only every be a partial one, as it is based on a circular argument). Recordings of these sounds, and similar predictions of possible splashdown

sounds, can be accessed via the web page[10]. Nevertheless, the inversion was conducted without reference to the higher order moments[11], and the associated discrepancies were evident in listening-test comparisons of the measured and reconstructed Salmon Leap data. In addition, whilst the general shape of the predicted spectrum for Titan agreed with back-of-the-envelope calculations[2] and appeared to be physically sensible, the absolute spectral levels seemed to be too high. Therefore this study set out to provide a more stringent inversion routine. Furthermore, a very different waterfall was chosen in order to test the general trends found in the first study (see section 3).

2.2 Theory

The method used to compute the bubble size distribution is an extension of the classical technique of Loewen and Melville[8]. This extension differs from the original approach in three ways: first a pair of measurements are exploited; second the contribution of each ringing bubble is not constrained to lie in a single frequency bin; third a monopole model for the bubbles is used because, despite the fact that the bubbles are entrained near the surface, the dipole model of Loewen and Melville is not suitable for our measurement geometry.

As with all acoustic inversion models one needs a forward model that predicts measurable acoustic quantities from physical parameters. There are several forward models that one might choose to exploit, depending upon the particular measurement geometry. Whilst the choice of model can significantly affect the results one obtains from a particular data set, it is not fundamental to the principle described herein. Therefore we will initially describe the technique in the absence of specifics relating to the forward model, and only later provide the details of the exact model employed to obtain our results. Thus we denote our forward model as follows:

$$p(t) = \Pi(t; t_0, r, h, R_0) = \Pi(t - t_0; r, h, R_0) \tag{1}$$

where $p(t)$ represents the measured pressure at the hydrophone, t_0 is the instant at which the pressure fluctuation from the bubble first arrives at the hydrophone, r is the range from hydrophone to the bubble, h is the entrainment depth, R_0 is the bubble's equilibrium radius and the function Π is simply a formal mechanism that relates the physical parameters to the measured time series. In the context of this paper, different forms of the function Π can be defined for Earth and Titan, which correspond to the differing environmental conditions. The measured pressure at the hydrophone is simply the sum of the contributions from all the bubbles, so that:

$$p_m(t) = \sum_{n=1}^{N} \Pi(t - t_{0,n}; r_n, h_n, R_{0,n}) \tag{2}$$

where the index n is included to indicate physical parameters of an individual bubble. If one assumes a spatially localised bubble cloud, characterised by a constant entrainment depth, then one can assume that r_n and h_n are independent of n; the notation r and h will be adopted for these fixed values. By using time-averaged quantities one is able to remove the temporal dependence in (2) and if these quantities obey a superposition principle then the structure of (2) remains unchanged. Specifically if the time-averaged operator is denoted $C\{\}$ then:

$$\Omega = C\{p_m(t)\} = \sum_{n=1}^{N} C\{\Pi(t - t_{0,n}; r, h, R_{0,n})\} \tag{3}$$

in which the assumption of a superposition principle for $C\{\}$ has been exploited. The most obvious choice for a general class of operators $C\{\}$ are temporal estimates of cumulants[12]. The second order cumulant relates directly to power. It should be noted that the superposition principle for cumulants requires that the bubble signatures are statistically independent. Whilst the second order cumulant is the obvious choice for this operator, the advantages of using higher order cumulants has been highlighted elsewhere[13]. In order to obtain a tractable solution based on (3) it is necessary to approximate the summation over all bubbles by a radius binned form, namely:

$$\Omega \approx \sum_{i=1}^{B} N(R_i)\chi(R_i, h, r) \qquad \chi(R_i, h, r) = \overline{C\{\Pi(t - t_0; h, r, R_0)\}} \tag{4}$$

The over-bar notation indicates that an average has been conducted over the values of R_0 in the i^{th} bin, R_i is the centre radius in the i^{th} bin, $N(R_i)$ is the number of bubbles in the radius bin and B is the number of bins. If the chosen operator is the second order cumulant (power) then χ reflects the average power of a bubble in a particular radius bin. The inversion method used by Loewen and Melville was simplified by use of the assumption that all of the energy contributed by bubbles in a given radius bin occurs at a particular frequency (the natural frequency of a bubble of radius R_i). Application of this assumption allows one to write:

$$\Omega(f_k) \approx N(R_i)\chi(R_i, h, r) \tag{5}$$

where $\Omega(f_k)$ is the value of $C\{p_m(t)\}$ once $p_m(t)$ has been band-pass filtered about f_k. Since values of χ can be readily estimated from the model, then (5) allows estimation of the number of bubbles. To obtain (5) one assumes that a given bubble only contributes to one frequency bin. This assumption is only reasonable if wide frequency bins are employed, specifically if the frequency bin width is significantly larger than the bandwidth of the bubble signature. As a result, this approximation provides a lower limit on the realisable resolution of the method. An alternative approach is to account for the contributions of bubbles in all frequency bins, so that (5) becomes:

$$\Omega(f_k) = \sum_{i=1}^{B} N(R_i)\tilde{\chi}(R_i, f_k) \tag{6}$$

in which $\tilde{\chi}(R_i, f_k)$ represents the contribution of bubbles in the i^{th} radius bin to the k^{th} frequency bin. One can employ equal numbers of frequency and radius bins, most conveniently arranged so that the frequencies map to the resonant frequencies of the bubbles with the specified radii. In such circumstances (6) represents a linear system of equations which can be solved using standard matrix methods. The reader is reminded that (6) is general in the sense that it applies to any operator $C\{\}$ with the stated properties.

When using the second order cumulant (which relates to power) then background noise can represent a significant problem. Specifically the value of $\Omega(f_k)$ is the addition of the power of the bubble signatures and the noise, leading to an overestimation of the number of bubbles. In the experiment presented here, we are able to mitigate against this by placing a hydrophone some distance from the localised source of bubble noise, allowing us to make an independent measurement of the background noise. This noise contains some contribution from the bubbles, an effect that can be further mitigated by replacing the temporal average used when computing $\Omega(f_k)$ with a temporal median. The median removes outlying values and can be corrected to provide a robust estimate of the mean[14]. This will be denoted as $\Omega_{noise}(f_k)$. Thus our power-based estimate of the bubble population is obtained, in matrix form, as:

$$\underline{N} = \tilde{\boldsymbol{\chi}}^{-1} \max\{\underline{\Omega} - \underline{\Omega}_{noise}, 0\} \tag{7}$$

where $\underline{N}$, $\underline{\Omega}$ and $\underline{\Omega}_{noise}$ are $B\times1$ column vectors and $\tilde{\boldsymbol{\chi}}$ is a matrix of values of $\tilde{\chi}(R_i, f_k)$. Inverses based on (7) rely on the numerical qualities of the matix $\tilde{\boldsymbol{\chi}}$. If the condition number in the matrix is large then the inversion will be sensitive to noise. In the passive inversion problem the conditioning of this matrix is not a fundamental problem, because the matrix does not have large off-diagonal terms. This is in contrast to inversions based on active bubble sizing problems where the matrix inversion is hindered by ill-conditioning[15]. The condition number of the matrix $\tilde{\boldsymbol{\chi}}$ only becomes problematic when small bin sizes are used. By suitable bin size selection one can avoid the need for regularisation. This is a fundamental restriction on bin sizes which is less stringent than that imposed by the assumption inherent in (5).

Having obtained a bubble population, the forward model (2) can then be used to synthesize time series for the bubble entrainment noise. To synthesize a measured hydrophone signal, one should also create a background noise signal with the characteristics of $\Omega_{noise}(f_k)$, which can be realised by filtering Gaussian white noise. To synthesize the noise of bubbles being entrained under different physical conditions, one simply needs to substitute the appropriate function Π during the synthesis process, *i.e.* implementation of (2).

2.3 Experiment

The data for our experiments were collected from a small waterfall on the Highfield campus of the University of Southampton, Southampton UK. The waterfall is one of several in a series along a creek passing through the centre of the campus, and is pictured in Figure 3(a). Two hydrophones were used to make acoustic observations: a Reson NUMBER (S/N 1999014) and a Bruel and Kjaer 8103 (S/N 2262868). Bruel and Kjaer Type 2635 charge amplifiers were used to deliver the signal to a 2-channel battery-powered Aiwa HHB 1 Pro DAT recorder recording at 44.1 kHz per channel. Anti-aliasing filters are incorporated into the DAT recorder device. DAT analogue output was captured to computer using an Edirol UA-1A USB audio interface using Adobe Audition. The acoustic centre of each hydrophone was 10 cm beneath the surface, with the closest sensor being approximately 50 cm from the waterfall and the second senor being 1.85 m. Recordings were made covering two configurations, with the positions of the two sensors being reversed. Underwater photos were taken to allow estimates of bubble entrainment depth to be formed. One such photo is shown in Figure 3(b).

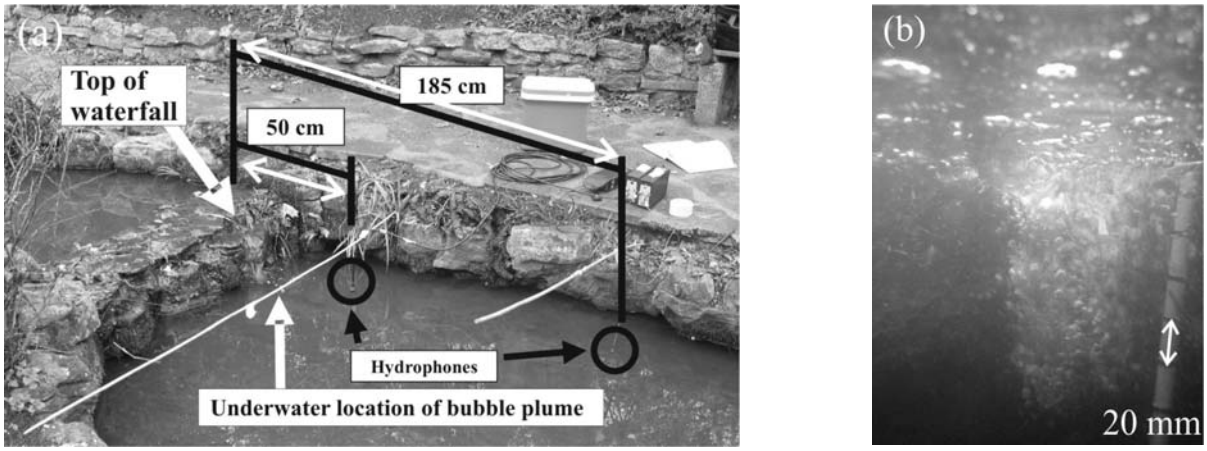

Figure 3. (a) Equipment layout during data capture in the creek on the Highfield Campus (University of Southampton). The vertical arrow shows location of bubble entrainment photographed underwater in (b), where the scale bar is based on the not-quite vertical measuring pole.

2.4 Results

The data corresponding to recordings made using the same hydrophone at the two locations were analysed. Figure 4(a) illustrates the power spectra computed in these locations. In the distance location median processing has been used to attenuate further the effect of the waterfall and to provide an improved estimate of the background noise. These spectra demonstrate that the dominant frequency band containing bubble entrainment noise is roughly 1-10kHz. Below 1 kHz the first order assumption is made that the signal is dominated by hydrodynamic noise from the waterfall (this can be tested using the fact that hydrodynamic signals attenuate at different rates to acoustic ones); and above 10 kHz the spectra are dominated by a non-bubble noise (characterised as such because of its similarity at both hydrophones). An inversion based on (7) was performed; using 5, 10, 15 and 20 radius bins in the frequency range 1-10 kHz. The results are shown in Figure 4(b) expressed in number of bubbles entrained per micrometer radius increment per second. The bubble distributions estimated in this manner show considerable consistency. The case where 20 radius bins are employed does show an oscillatory behaviour and does generate a negative bubble populations for one bin, highlighting the fact that for this choice of bin size the $\tilde{\chi}$ matrix is becoming ill-conditioned.

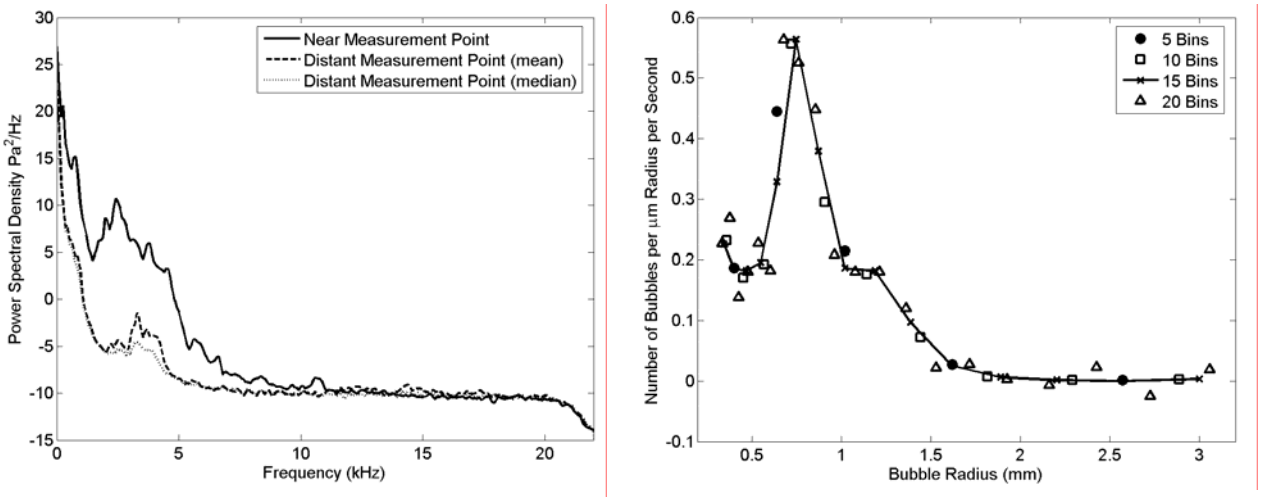

(a) (b)

Figure 4. (a) Power spectra computed from data measured at two locations shown in Figure 3, expressed in dB. (b) Inversions results for different numbers of size bins.

Data from this inversion were then used to synthesize the original recordings and so produce a test dataset that can be used for algorithmic validation. Figure 5(a) shows four sets of results, those for an inversion based on (7), that are based on acoustic power, and results based on (6) in which the fourth order cumulant (the kurtosis) has been used. Since the fourth order cumulant is unaffected by additive Gaussian noise then there is no need to form a separate estimate of the background noise contribution, so (6) can be solved directly. For the synthetic data the fourth order inversion agrees with results for the power based method (using the measured and synthetic data sets). However the inversion for the fourth order scheme provides a large overestimate of the bubble population when applied to the measured data. These results are consistent for different bins sizes (results not shown here), demonstrating that this is not a consequence of ill-conditioning. The fact that the fourth order inversion scheme functions correctly on the synthesised data provides confidence that it is algorithmically correct. This leads one to suggest that the model on which the method is based is in some sense incomplete. Listening to the synthesised data provides further evidence for this. The synthetic and measured data have the same power spectrum (which is a necessary condition for the inversion from the synthetic data to match the results from the measured data, see Figure 5(a)). Despite this spectral equivalence the subjective quality of the synthetic signal is quite different to the measured signal as was observed for the data from Salmon Leap[2].

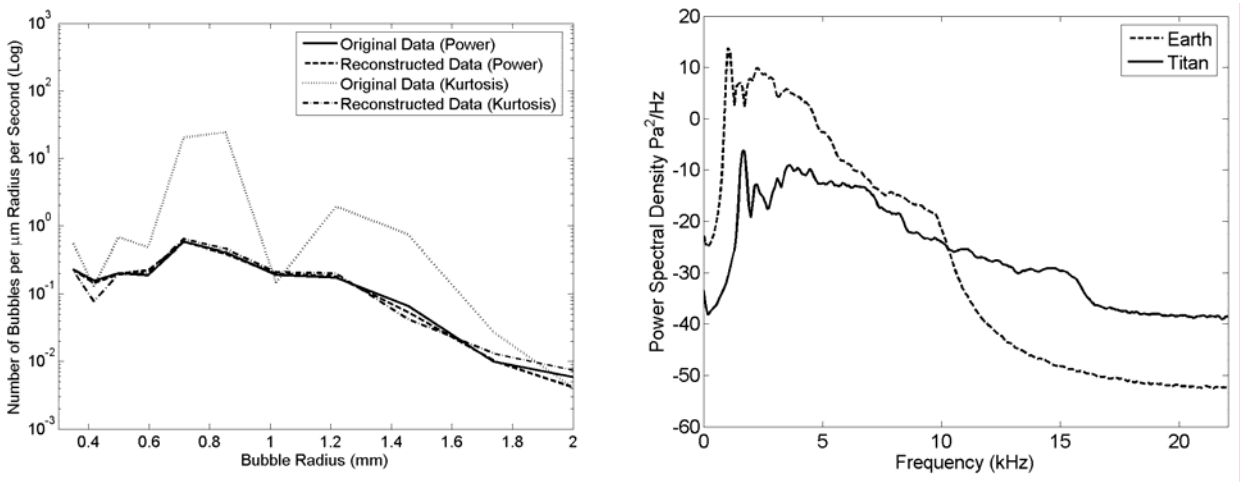

(a) (b)

Figure 5. (a) Estimated bubble populations. (b) Power spectral densities for bubble entrainment noise, expressed in dB.

Figure 5(b) shows the power spectral densities computed using the data obtained by inverting bubble size distributions measured on Earth; but during the inversion the environmental parameters for Titan are employed. Thus one obtains a prediction for the sound of a methane-fall on Titan. It can be seen from Figure 5(b) that the general effect is to shift the spectrum upwards in frequency, creating a higher pitched sound, confirming the trend of the earlier paper[2]. However this improved method removes the high spectral levels judged to be unreliable in the predictions of the earlier paper[2], and shows a more physically realistic reduction in the overall signal power (~17 dB).

2.5 Discussion of results for Titan

This paper has outlined an advance on the existing techniques for inverting the entrainment emissions of bubbles, and applied it to estimate the sounds of methane-falls on Titan. Whereas the initial study[2] estimated spectral levels on Titan that were ~10 dB greater than the terrestrial values, refinement of the assumptions associated with the excitation predicts similar levels for the two (Figure 5(b)). The general shift in energy to higher frequencies is very similar in both studies, and to be expected from back-of-the-envelope calculations[2]. In its descent, *Huygens* photographed features which are currently believed to reflect the presence of flowing liquid on Titan (Figure 6(a),(b)), which carves out valleys and presumably is likely to generate methane-falls. The landing site, though possibly close to such an area (Figure 6(c)), is thought to be on a mud- or snow-like surface, and hence the microphone on the probe did not detect the sound of either a methane-fall or a splashdown. Such a methane-fall might resemble that depicted in Figure 1(a), falling into a crater sea on Titan. Sounds of splashdowns and methane-falls are available at the website[8].

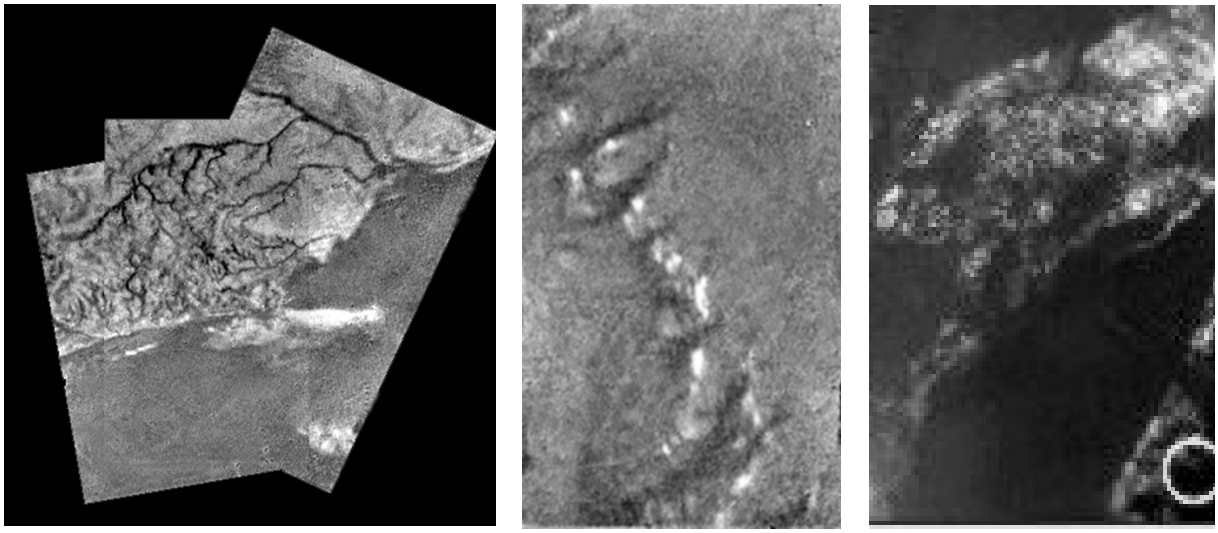

(a) (b) (c)

Figure 6. Images of Titan obtained by the Huygens probe. (a) This mosaic of three frames provides detail of a high ridge area including the flow down into a major river channel from different sources. (b) A single image from the Huygens DISR instrument of a dark plain area on Titan, seen during descent to the landing site. There appears to be flow around bright 'islands'. The areas below and above the bright islands may be at different elevations. (c) The landing site of Huygens is circled. (Credits: ESA/NASA/JPL/University of Arizona)

The purpose of this exercise is to demonstrate the opportunities which acoustic measurements offer for space exploration. The signal has low bandwidth, the hardware is rugged, and typically has low mass, low cost, and low power requirements. Given the myriad uses for diagnosis by bubble-generated sound on Earth, from rainfall sensing to investigating atmosphere/ocean mass flux, this exercise illustrates that the use of sound in general as an extraterrestrial diagnostic presents intriguing possibilities. This issue is examined further in section 3.

3 EUROPA

Is there a future for acoustics in space exploration? Whilst the applications would not be restricted to those relating to oceans in space, nevertheless the next venture which seems possible is to Europa. Discovered in 1610 by Galileo Galilei and having a mean radius of 1561 km (i.e. 0.245 that of Earth, extending to 1569 km at the equator), Europa is a little smaller than Earth's moon. It is made primarily of silicate rock with, probably, a core of metallic iron, and has a mean density of $\rho_E = 3013$ kg m^{-3}. There is a very faint atmosphere of oxygen, with a surface atmospheric pressure of 1 μPa, and a surface temperature of ~103 K (min: ~50 K; max: 125 K). Europa's icy surface is criss-crossed with coloured lines up to ~20 km wide (Figure 7(a)). These indicate cracks, generated by Jupiter's tidal forces (which generate differences of up to 30 m between high and low tides). Warmer material from beneath wells up as a result of volcanic water eruptions from cryovolcanoes, bringing with them minerals which discolour the ice. Whilst Earth's atmospheric oxygen has biological origins, on Europa it is probably generated through the production of water vapour (which is subsequently split into oxygen and hydrogen, the latter being light enough to then escape Europa's gravity) by the interaction of charged particles and sunlight with Europa's ice.

However Europa is in synchronous orbit around Jupiter (the rotational and orbital periods both equalling 3.551181 Earth days), and passes through that planet's massive gravitational and magnetic fields. On 2 March 1998 NASA announced that magnetic field data from the *Galileo* orbiter indicated that Europa generates an induced magnetic field through interaction with Jupiter's field. Probably the most likely explanation for this in such circumstances would be the presence of a subsurface conductive layer, most probably a salty liquid-water ocean. Therefore is it probable that, beneath a covering of perhaps 10-30 km ice, there is a sea of possibly 100 km depth of water, heated through the interactions with Jupiter which cause tidal and seismic activity (Figure 7(b)). When one considers that Earth's Artic sea ice is typically only around 3 m thick (at time of writing), and the seabed is at a depth of up to 1038 m (the Arctic is the smallest and shallowest of the World's five oceans) the difficulties in sending a vehicle to explore Europa's seas appears to be very considerable. Even with the reduced gravity of Europa (at 1.31 m/s^2, approximately 13% that of Earth), the hydrostatic pressures would be enormous (several thousand bar at the base of the water column, noting to include the effect of the ice). For example, the 4 x 10^8 Pa which can be calculated from equation (14) for the pressure at the base of the water column (assuming the parameter values given with equation (14)) is equivalent to that which would be found on Earth under 40 km of water. Current undersea technology cannot achieve these depths on Earth. However this is what has been proposed (Figure 8), driven in part by the possibility of finding life fuelled by hydrothermal vents (as are found in Earth's seas).

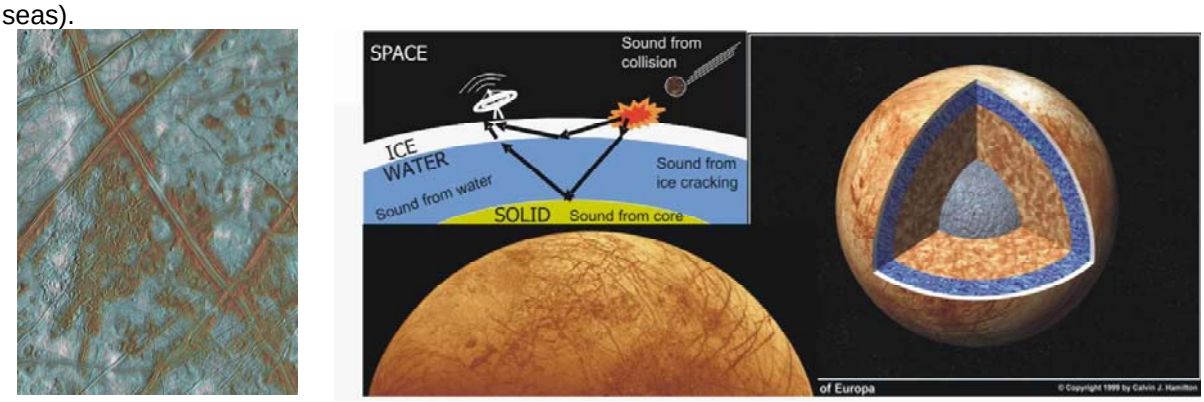

(a) (b)

Figure 7. (a) Cracks on Europa's ice surface. Most scientists believe that salts and other inorganic materials are responsible for the coloured patches on Europa's outer layer, although there has been speculation that bacteria, extruded through the ice from below and 'flash frozen' on the surface, are responsible. (Credit: NASA/JPL) (b) Top left: schematic of possible acoustic-based mission to Europa, where acoustic signals originating from various planetary sources are passively detected and transmitted to Earth via an orbiter (schematic: TG Leighton). Lower: the surface of Europa, showing ice features (Credit: NASA/JPL). Right: Schematic of the interior of Europa, showing ice covering over a water ocean, overlaying the solid interior (Copyright Calvin J Hamilton).

Communication through such distances of water and ice could require the use of acoustics. However acoustics offers an intriguing alternative to attempting to burrow or melt a vehicle through so much ice, and then maintaining contact through such deep water. Probe acoustic signals could be propagated through the ice. A cheaper alternative (in terms of power consumption) would be to exploit passive acoustic sensing only, and analyse 'signals of opportunity', such as might be made by geophysical processes (ice cracking, meteorite collisions *etc*). Certainly it would be easier to 'let the signals come to the sensor' rather than try to send a vehicle to the ocean depths on Europa.

Figure 8. Artist's conception of a submersible vessel exploring a liquid ocean beneath Europa's surface. The scenarios would envisage a large nuclear powered "Melt Probe" (cryobot) which would melt through the ice, avoiding obstacles. Once it reached the water, it would deploy an autononomous underwater vehicle (hydrobot), which would gather information and send it back to Earth. In this rendition, the vessel's light is illuminating a hydrothermal vent where, NASA hopes, lifeforms (possibly resembling terrestrial extremophile bacteria) possibly could live (none of the known terrestrial extremophile bacteria could survive the harsh conditions of Europa's surface). The figure shows the hydrobot in the foreground, with the melt probe penetrating the ice covering the background. Several features in the image are unlikely, including the distance between the base of the ice and the seabed, and the level of ambient light. (Credit: NASA).

It is possible to estimate some of the transmission characteristics of Europa's seas. The sound speed in Earth's oceans has been characterised by several similar empirical equations. Adaptation of the terrestrial formulation[16] of one of these gives the following equation for the sound speed (c /m s^{-1}) in the ocean as a function of temperature (T /°C), salinity (S , in parts per thousand), acceleration due to gravity (g /m s^{-2}) and ocean depth (z /m):

$$c = 1449.2 + 4.6T - 0.055T^2 + 0.0003T^3 + (1.39 - 0.012T)(S - 35) + 1.74 \times 10^{-6} \times P_{\mathrm{h}} \qquad (8)$$

where the densities of both water (ρ_w) and ice (ρ_{ice}) are measured in density kg m^{-3}. In (8), P_{h} is the hydrostatic pressure. Assume that the ice has thickness h_{ice}. It is not precise to say that $P_h = g(\rho_w z + \rho_{ice} h_{ice})$ at some depth z below the base of the ice. To do so would be to assume a constant acceleration due to gravity, and to ignore the curvature of the moon's spherical geometry (the assumption of constant densities for the water and ice is maintained throughout this section). Let us rather discuss the separate components that make up the hydrostatic pressure. We assume an almost zero atmospheric pressure, and ocean depth z is measured positively downwards from the base of the ice.

Whilst on Earth it is usual to ignore the difference in the acceleration due to gravity from surface to the seabed, the effect is much larger on Europa because it is a smaller planetary body, and because the sea depths are so much greater. Given a gravitational constant of $G = 6.67300 \times 10^{-11}$ m^3 kg^{-1} s^{-2}, $\rho_{\mathrm{E}} = 3013$ kg m^{-3}, and assuming the top of the ice forms a sphere of mean radius $R_{\mathrm{outer}} = 1561$ km, the acceleration due to gravity at the seabed is found approximately by:

$$g_{\mathrm{seabed}} \approx \frac{4G\pi R_{\mathrm{bed}}^3}{3R_{\mathrm{bed}}^2}\rho_{\mathrm{E}} = \frac{4G\pi R_{\mathrm{bed}}}{3}\rho_{\mathrm{E}} \approx 1.214 \text{ m s}^{-2}. \tag{9}$$

where the distance of the seabed from the centre of the moon is $R_{\mathrm{bed}} \approx R_{\mathrm{outer}} - 120 \quad \mathrm{km} \approx 1441$ km (Figure 9).

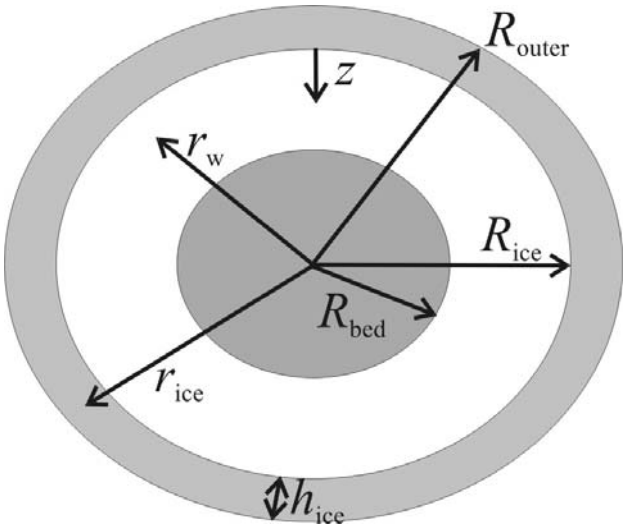

Figure 9. Cross-section of Europa labelling key fixed ($R_{\mathrm{bed}}, R_{\mathrm{ice}}, R_{\mathrm{outer}}$) and variable ($r_{\mathrm{w}}, r_{\mathrm{ice}}$) radii.

Clearly if one considers the acceleration due to gravity at a spherical surface, centred on the moon's centre, then as the radius of that surface increases it moves further from the centre of the moon. During this process, the distance between the surface and the moon's centre increases, which would tend to reduce the acceleration due to gravity. This effect is countered by the additional mass which is encompassed within the volume mapped out by that spherical surface. The net effect on the gravity will depend on the densities through which the spherical surface passes as it moves away from the centre.

At a location in the water, a distance r_{w} from the moon's centre, the acceleration due to gravity is:

$$g(r_{\mathrm{w}}) \approx \frac{G}{r_{\mathrm{w}}^2}\left(\frac{4\pi R_{\mathrm{bed}}^3\rho_{\mathrm{E}}}{3} + \int_{R_{\mathrm{bed}}}^{r_{\mathrm{w}}} \rho_{\mathrm{w}} 4\pi r^2 \mathrm{d}r\right) = \frac{4\pi G}{3r_{\mathrm{w}}^2}\left(r_{\mathrm{w}}^3\rho_{\mathrm{w}} + R_{\mathrm{bed}}^3\left(\rho_{\mathrm{E}} - \rho_{\mathrm{w}}\right)\right). \tag{10}$$

Similarly, at a location in the ice, a distance r_{ice} from the moon's centre, the acceleration due to gravity is:

$$g(r_{\mathrm{ice}}) \approx \frac{4\pi G}{3r_{\mathrm{ice}}^2}\left(\left(R_{\mathrm{ice}}^3 - R_{\mathrm{bed}}^3\right)\rho_{\mathrm{w}} + R_{\mathrm{bed}}^3\rho_{\mathrm{E}} + \left(r_{\mathrm{ice}}^3 - R_{\mathrm{ice}}^3\right)\rho_{\mathrm{ice}}\right). \tag{11}$$

From (11), the value of the gravity at the surface of the moon is 1.31 ms^{-2}, in agreement with the values in the literature.

In what follows, the number of significant figures quoted with numerical values does not reflect confidence in the accuracy of those values. Rather, it represents the precision required to distinguish estimates obtained from the following analysis, from those which are given for comparison following 'back-of-the-envelope' calculations.

Hence the total weight of ice on Europa is

$$W_{\text{ice}} = \rho_{\text{ice}} \int_{R_{\text{ice}}}^{R_{\text{outer}}} 4\pi r^2 g(r)\,\mathrm{d}r\,, \tag{12}$$

where within the integral, $g(r_{\text{ice}})$ from (11) is used for $g(r)$. This comes to 7.35 x 10^{20} N. This weight can be compared with that obtained by assuming a constant value for the acceleration due to gravity, taking the value at the surface (g_{s}=1.31 m/s^2), which is $4\pi\rho_{\text{ice}} g_{\text{s}} (R_{\text{outer}}^3 - R_{\text{ice}}^3)/3$=7.29 x 10^{20} N (for $R_{\text{outer}} = 1561$ km, $R_{\text{ice}} = 1541$ km, ρ_{ice} = 920 kg m^{-3}). This provides a hydrostatic pressure at the base of the ice sheet of $P_{\text{ice}} = W_{\text{ice}}/(4\pi R_{\text{ice}}^2)$ = 24.6 MPa. This can be compared to the pressure estimated by taking the approximate weight of the ice calculated above (7.3 x 10^{20} N) and dividing it by the surface area of the base of the ice, $4\pi R_{\text{ice}}^2$=2.98 x 10^{13} m^2, which gives a hydrostatic pressure of 24.4 MPa. A hydrostatic pressure of 1 bar would be encountered at a depth of about 82.9 m below the outer surface of the ice.

In similar vein, consider a spherical shell of radius r_{w} centred on the moon's core. The weight of water on that shell is:

$$W_{\text{w}} = \rho_{\text{w}} \int_{r_{\text{w}}}^{R_{\text{ice}}} 4\pi r^2 g(r)\,\mathrm{d}r\,, \tag{13}$$

where within the integral, $g(r_{\text{w}})$ from (10) is used for $g(r)$. Therefore the hydrostatic pressure equals the sum of weights of water and ice upon it, divided by the area of this surface $4\pi r_{\text{w}}^2$:

$$\begin{aligned}
P_{\text{h}}(r) &= \frac{W_{\text{ice}} + W_{\text{w}}}{4\pi r_{\text{w}}^2} = \frac{W_{\text{ice}} + \rho_{\text{w}} \int_{r_{\text{w}}}^{R_{\text{ice}}} 4\pi r^2 g(r)\,\mathrm{d}r}{4\pi r_{\text{w}}^2} \\
&= \frac{W_{\text{ice}} + \rho_{\text{w}} \int_{r_{\text{w}}}^{R_{\text{ice}}} 4\pi \frac{4\pi G}{3}\left(r^3\rho_{\text{w}} + R_{\text{bed}}^3\left(\rho_{\text{E}} - \rho_{\text{w}}\right)\right)\mathrm{d}r}{4\pi r_{\text{w}}^2} \\
&= \frac{W_{\text{ice}}}{4\pi r_{\text{w}}^2} + \frac{\rho_{\text{w}} \int_{r_{\text{w}}}^{R_{\text{ice}}} \frac{4\pi G}{3}\left(r^3\rho_{\text{w}} + R_{\text{bed}}^3\left(\rho_{\text{E}} - \rho_{\text{w}}\right)\right)\mathrm{d}r}{r_{\text{w}}^2} \\
&= \frac{W_{\text{ice}}}{4\pi r_{\text{w}}^2} + \frac{\rho_{\text{w}} \frac{4\pi G}{3} R_{\text{bed}}^3\left(\rho_{\text{E}} - \rho_{\text{w}}\right)\left(R_{\text{ice}} - r_{\text{w}}\right)}{r_{\text{w}}^2} + \frac{\rho_{\text{w}}^2 \int_{r_{\text{w}}}^{R_{\text{ice}}} \frac{4\pi G}{3} r^3\,\mathrm{d}r}{r_{\text{w}}^2} \\
&= \frac{W_{\text{ice}}}{4\pi r_{\text{w}}^2} + \frac{\rho_{\text{w}} \frac{4\pi G}{3} R_{\text{bed}}^3\left(\rho_{\text{E}} - \rho_{\text{w}}\right)\left(R_{\text{ice}} - r_{\text{w}}\right)}{r_{\text{w}}^2} + \frac{\rho_{\text{w}}^2 \frac{4\pi G\left(R_{\text{ice}}^4 - r_{\text{w}}^4\right)}{12}}{r_{\text{w}}^2}\,.
\end{aligned} \tag{14}$$

Assuming the water is 100 km deep, and the ice 20 km, equation (14) can readily be expressed in terms of z for use in an empirical form of (8) which allows for the variation in gravity with depth:

$$c = 1449.2 + 4.6T - 0.055T^2 + 0.0003T^3 + (1.39 - 0.012T)(S - 35) \qquad (15)$$
$$+1.74\times10^{-6} \times \left(\frac{W_{\text{ice}}}{4\pi r_{\text{w}}^2} + \frac{\rho_{\text{w}} \dfrac{4\pi G}{3} R_{\text{bed}}^3 \left(\rho_{\text{E}} - \rho_{\text{w}}\right)\left(R_{\text{ice}} - r_{\text{w}}\right)}{r_{\text{w}}^2} + \frac{\rho_{\text{w}}^2 \dfrac{4\pi G\left(R_{\text{ice}}^4 - r_{\text{w}}^4\right)}{12}}{r_{\text{w}}^2} \right)$$

Equation (15) implies that the sound speed will increase with depth, and therefore acoustic propagation in the ocean will be upwardly refracting. This can be seen from Figure 10.

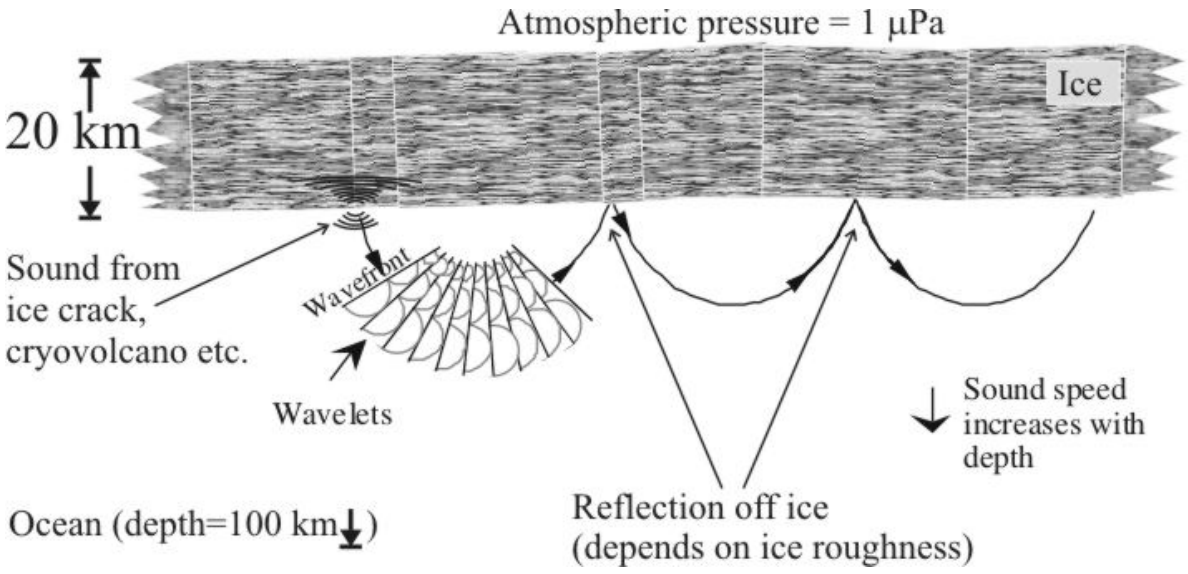

Figure 10. Schematic of the refraction and reflection of sound. A source of sound at the base of the ice field emits into both water and ice. The ocean is upwardly refracting. This can be seen from the Huygens' wavelet construction. As a result, the sound returns to the ice from where it is reflected (with fidelity depending on the smoothness of the ice), to continue along the ocean through subsequent refraction and reflections.

Equation (15) could be used to quantify this effect. However for the purposes of this feasibility study, a simpler, more approximate sound speed variation will be used. To introduce this approximation and to indicate the error associated with it used, consider the following scenario. Given that adequate data on Europa's seas are not available, the following input will be used: a region of ocean 10^5 m deep, where the salinity is uniform at 35 parts per thousand, and the temperature uniform at 0°C. For Europa, ρ_w =1000 kg m^{-3}. Given that we know that eleven different forms of crystalline ice can be generated on Earth, and given the low surface temperatures, an estimated value of ρ_{ice} is taken to be 920 kg m^{-3}. The approximation of constant densities is made. This formulation will now be employed to determine the path of a ray projected horizontally at the surface in a model region of the ocean. Substitution of these values into (15) gives:

$$c = 1449.2 + 1.74\times10^{-6}\times\left(\frac{W_{\text{ice}}}{4\pi r_{\text{w}}^2} + \frac{\rho_{\text{w}}\dfrac{4\pi G}{3}R_{\text{bed}}^3\left(\rho_{\text{E}}-\rho_{\text{w}}\right)\left(R_{\text{ice}}-r_{\text{w}}\right)}{r_{\text{w}}^2} + \frac{\rho_{\text{w}}^2\pi G\left(R_{\text{ice}}^4 - r_{\text{w}}^4\right)}{3r_{\text{w}}^2}\right) \quad (16)$$

Substituting for $r_{\text{w}} = R_{\text{ice}} - z$ in (16) gives:

$$c = 1449.2 + 1.74\times10^{-6}\times\left(\frac{W_{\text{ice}}}{4\pi(R_{\text{ice}}-z)^2} + \frac{\rho_{\text{w}}\dfrac{4\pi G}{3}R_{\text{bed}}^3\left(\rho_{\text{E}}-\rho_{\text{w}}\right)(z)}{(R_{\text{ice}}-z)^2} + \frac{\rho_{\text{w}}^2\pi G\left(R_{\text{ice}}^4 - (R_{\text{ice}}-z)^4\right)}{3(R_{\text{ice}}-z)^2}\right) \quad (17)$$

A plot of the sound speed prediction of equation (17) as a function of z shows that the sound speed increases approximately linearly with depth. This result is confirmed by a small-amplitude expansion of equation (17). Such a result would be expected from a simple-minded approach which ignores the variation of gravity with depth, and the effect of the curvature of the planet. That is to say, the approach assumes that the moon is large enough, and the oceans shallow enough, to assume throughout the water and ice that the acceleration due to gravity takes a constant value (equal to the surface value of g_{s} =1.31 m/s^2), and that the surfaces of constant hydrostatic pressure are planar (not spherical, as in (14)). These are assumptions which are used throughout terrestrial ocean acoustics. With such assumptions $P_{\text{h}} = g_{\text{s}}(\rho_{\text{w}} z + \rho_{\text{ice}} h_{\text{ice}})$ and the sound speed can be modelled from (8) as:

$$c = 1449.2 + 4.6T - 0.055T^2 + 0.0003T^3 + (1.39 - 0.012T)(S-35) + 1.74\times10^{-6} g_{\text{s}}(\rho_{\text{w}} z + \rho_{\text{ice}} h_{\text{ice}}) \quad (18)$$

Using the same environmental parameters as before, but now with g_{s} =1.31 m/s^2 and h_{ice} = 20 km, equation (18) reduces to a form where the sound speed will explicitly increase linearly with increasing depth:

$$c = 1449.2 + 1.74\times10^{-6}\times1.31(1000z + 1.84\times10^7) \approx 1491.1 + 0.00228z\,. \quad (19)$$

Given that the maximum difference in the sound speed predicted by (19) and (17) is less than about 2%, the model predictions for Europa for the remainder of this paper will use equation (19) to describe the sound speed profile.

The scenario where the sound speed varies linearly with depth will be very familiar to many acoustical oceanographers. In such circumstances, acoustic rays follow paths which are the arcs of circles. Consider Figure 11. A sound ray is initially travelling horizontally, passing through point X_{i} at a depth d_{i} with speed c_{i}. It then passes through point X_1 at a depth $z = d_1$ with speed c_1, and then passes point X_2 at a depth d_2 with speed c_2. If this is an acoustic ray which follows an arc of a circle, then two conditions must be satisfied. First, if the ray follows a circle arc, the circle has radius r_{c} such that the distance $L_{1,2}$ on the figure is:

$$L_{1,2} = r_{\text{c}}\cos\theta_1 - r_{\text{c}}\cos\theta_2 = d_1 - d_2\,. \quad (20)$$

Since the sound speed variation is linear with depth, then:

$$\frac{\partial c}{\partial z} = \frac{d_1 - d_2}{c_1 - c_2}\,. \quad (21)$$

Second, if the circle arc is a ray, Snell's Law must be satisfied. Snell's law allows statement of the relation between the sound speed at a particular depth and the angle, θ, which a ray at that depth makes locally with the horizontal:

$$\cos\theta_i / c_i = 1/c_i = \cos\theta_1 / c_1 = \cos\theta_2 / c_2 . \quad (22)$$

Equating $d_1 - d_2$ in (20) and (21), and substituting for the cosine terms using (22), indicates that the ray is following an arc of a circle that has radius

$$r_c = \frac{c_i}{\partial c / \partial z} . \quad (23)$$

Using (19) we can estimate that a ray which is travelling horizontally at depth $z = d_i$ follows the arc of a circle of radius

$$r_c \approx \frac{1491.1 + 0.00228 d_i}{0.00228} \approx d_i + 654 \quad \text{km} . \quad (24)$$

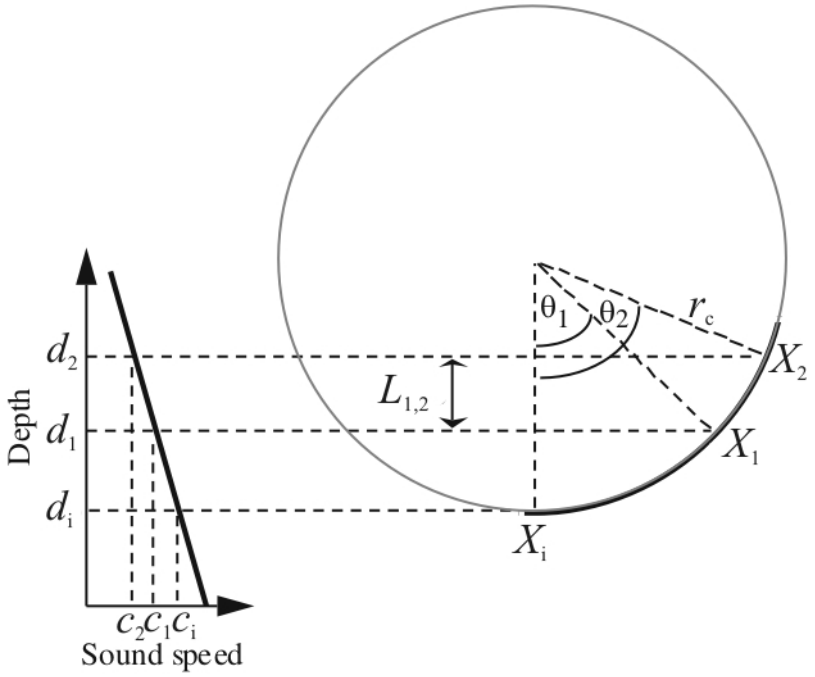

Figure 11. Ray paths in a region of ocean where the sound speed increases linearly with depth

The following estimates all are given acknowledging that they are approximate answers owing to the limitations of the model (constant gravity and an assumption of planar surfaces which neglects the curvature of the moon's geometry). The number of decimal places does not reflect the accuracy of the calculation. Rather the decimal places are retained to avoid unnecessary errors arising because these calculations are based on the effects of small differences between large numbers. If therefore an acoustic ray is projected horizontally from a sound source at depth 50 km in Europa's seas, the angle at which the ray intercepts the ice is readily calculated. From (19) the sound speed at this depth is $1491.1 + 0.00228 \times 50 \times 10^3 \approx$ 1605.1 m s^{-1}, and the sound speed at the boundary with the ice is 1491.1 m s^{-1}, so from (22) the ray meets the ice at an angle to the horizontal of

$\cos^{-1}(1491.1/1605.1) \approx 21.7^\circ$ according to this model. Similarly, from (22) a ray released from the surface at an angle of 30° will attain a horizontal trajectory when the sound speed is $(1491.1/\cos 30^\circ) \approx 1721.8$ m s^{-1}, which from (19) occurs at a depth of $(1721.8-1491.1)/0.00228 \approx$ 101.202 km. Since we have assumed an ocean depth of 100 km, this ray will intersect the seabed at a very shallow angle: indeed the angle of release for a ray which will just graze the seabed (i.e. be horizontal at a depth of 100 km where, from (19) the sound speed is $1491.1+0.00228\times10^5 \approx 1719.1$ m s^{-1}) is, from (22) $\cos^{-1}(1491.1/1719.1) \approx 29.85^\circ$. It follows the arc of a circle of radius 754 km (from (24) and, as is evident from Figure 12, the ocean depth equals $r_c(1-\cos\theta_g)$ where θ_g is the angle to the horizontal at the ice of the ray which just grazes the seabed ($\approx 29.8^\circ$ here)). From Figure 12, the ray will travel a horizontal distance of $2r_c \sin\theta_g \approx$ 750.6 km before it touches the ice again: therefore it would only take about 13 bounces (according to this model) before the ray has circumnavigated the moon's 9800 km circumference and returned to its point of origin. With a trajectory of $2r_c[\theta_g / \text{radians}] \approx$ 786 km, the ray would take around 2 hours to circumnavigate the moon.

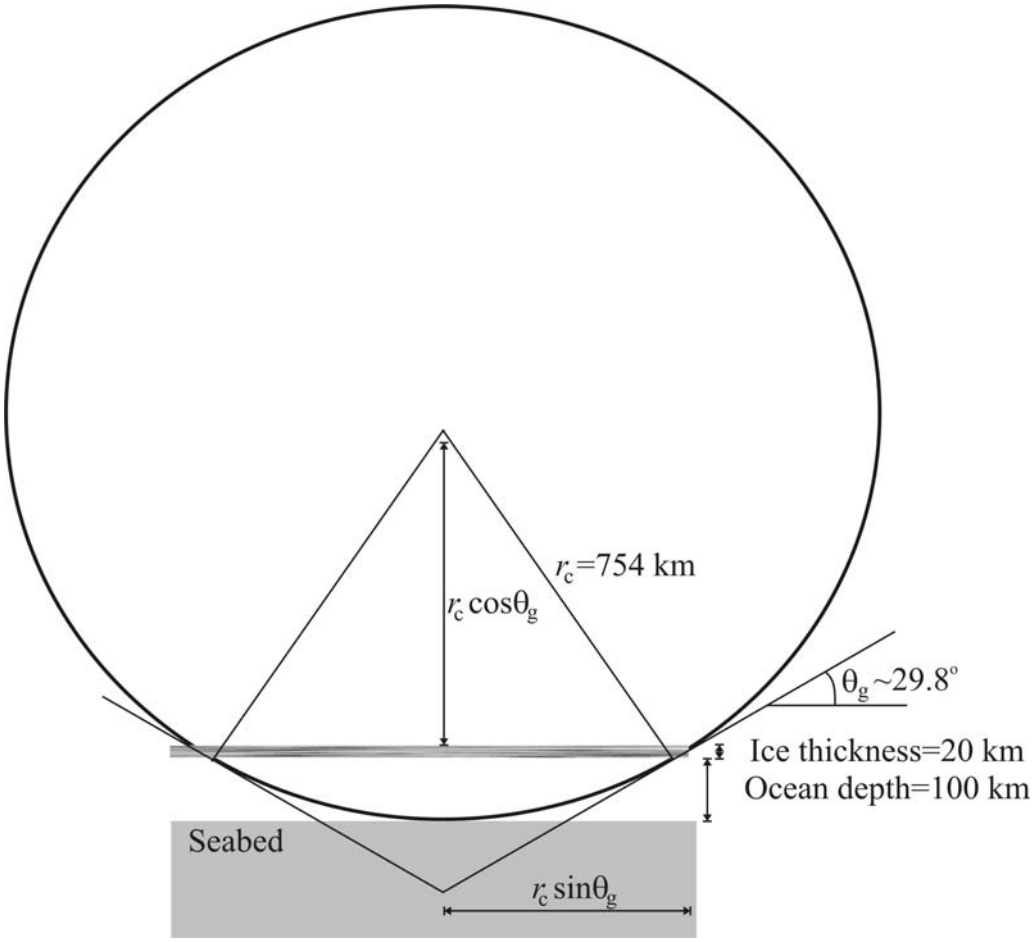

Figure 12. A ray, travelling from the surface to the position of its deepest descent, and then back to the 1000 m depth, within the model ocean profile (the radii of curvature are shown much reduced for clarity).

The accuracy of these simple estimates can be investigated through ray tracing, after the manner using by Leighton et al.[17] to study the acoustics of the bubble nets of humpback whales (Figure 13), in which:

$$\frac{dx}{ds} = c\xi(s), \tag{15}$$

$$\frac{d\xi}{ds} = -\frac{1}{c^2}\frac{dc}{dx} \tag{16}$$

$$\frac{dy}{ds} = c\varsigma(s) \tag{17}$$

$$\frac{d\varsigma}{ds} = -\frac{1}{c^2}\frac{dc}{dy} \tag{18}$$

Two stages of computation are undertaken:

- First, the computational ray tracing method was first used to confirm the analytical case, where the sea-bed, the sea-ice interface, and the isothermal lines are all straight parallel lines; essentially modelling Europa as a flat surface. The approximation that uses a constant gravity is maintained.

- Second, the curvature of Europa was then incorporated into the computational model. In this simple model, the acoustic field analysed is a circular duct. Neither potential deviations from sphericity nor horizontal gradients have been incorporated, though such effects have been shown to have a profound effect on Earth[18].

In the proposed seas of Europa a linear sound speed profile has been assumed as stated in equation (19). The upper boundary at the sea-ice interface was modelled as a rigid-wall. The lower boundary limit was estimated as being 100 km below the sea-ice interface, and was assumed to be completely absorbent.

For the first case modelled, a source was placed at the base of the ice sheet, emitting energy into the ocean below. The signal is refracted back towards the ice boundary, and then is reflected back into the water as shown in Figure 13. This cycle repeats.

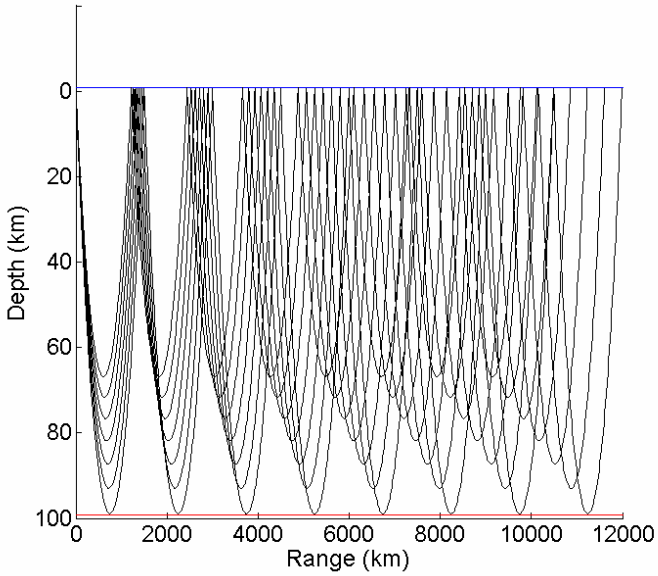

Figure 13. Rays emitted from a beam emitting energy from 25^o-29.8^o below the horizontal. As expected, each ray which is not absorbed at the sea bottom traces the arc of a circle. Each ray is only plotted for 9 reflections. The energy projected at ~29.8^o is the deepest-travelling refracted ray which completes the half-circle arc. Caustics are visible.

Consider that ray which just grazes the seabed before returning to the sea-ice interface. According to the zero-curvature model, this ray of deepest descent has a departure angle from the sea-ice interface of 29.84° below horizontal (compared to the 29.85° predicted after Figure 11). For this ray-path, the computational model showed the range between surface reflections to be on the order of 750 km. Since the radius of the Earth is about four times that of Europa, the zero-curvature assumption which works well for most ocean acoustics on Earth is not valid for Europa. The considerable curvature of Europa caused by its small radius, together with the vast 100 km ocean depth, combine to dictate that the zero-curvature model is not a reasonable approximation for acoustic propagation within its envisaged oceans. This is illustrated in Figure 14, where the curvature of the sea bottom is shown with respect to the flat surface approximation.

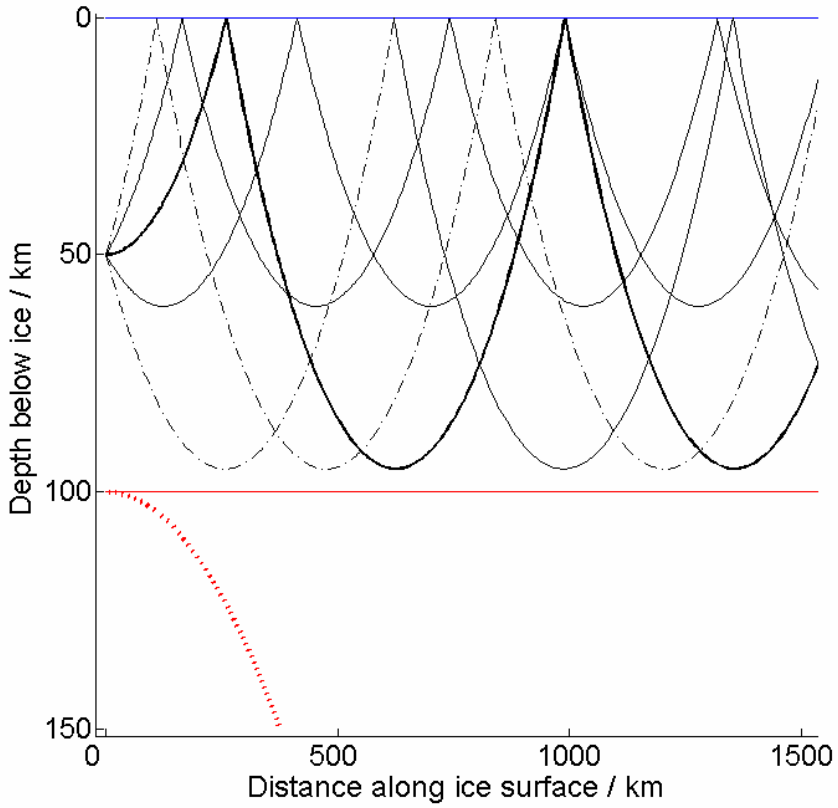

Figure 14. A ray plot showing (as a solid red line) the location of the seabed as assumed in this 'zero-curvature' model. The dotted red line shows on this scale the actual location of the seabed, assuming it curves to follow the geometry of a sphere centred at the moon's core (the curvature of the ice is not shown: the blue line indicates the position of the base of the ice in the 'zero-curvature' model). This illustrates the error which will be caused if the curvature of Europa is neglected from the model. The source of acoustic energy in this depiction is in the centre of the water column. The lower dotted line does not appear circular in this plot for the same reason that they ray arcs do not - the axes are not plotted on an equal scale.

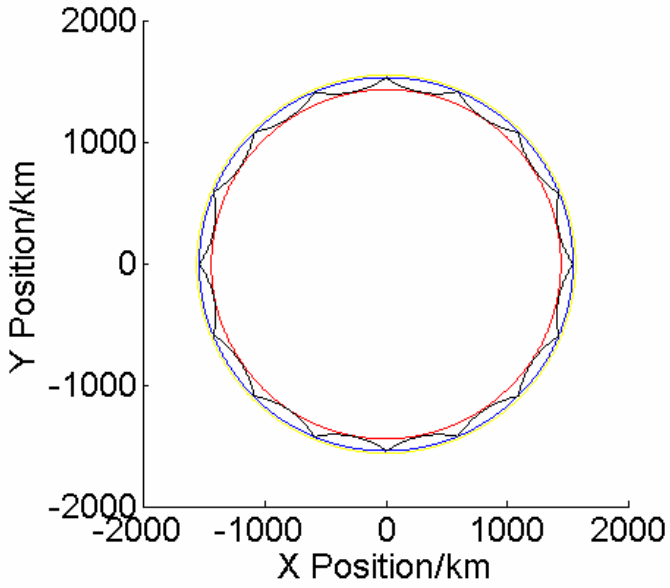

Figure 15. A ray emitted at 32.5^{o} below the horizontal will be reflected off the sea-ice boundary 15 times before returning to the receiver. This is the ray which does this with the minimum number of reflections. Other lower angles can be used to obtain similar results but require more reflections before they finally return to the source.

Figure 15 shows the path of that ray which propagates around Europa, to return to its point of origin with the minimum number of bounces from the base of the ice pack. Figure 16 shows the paths of rays from a range of launch angles. These calculations have a vertical axis of rotational symmetry for assumed conditions.

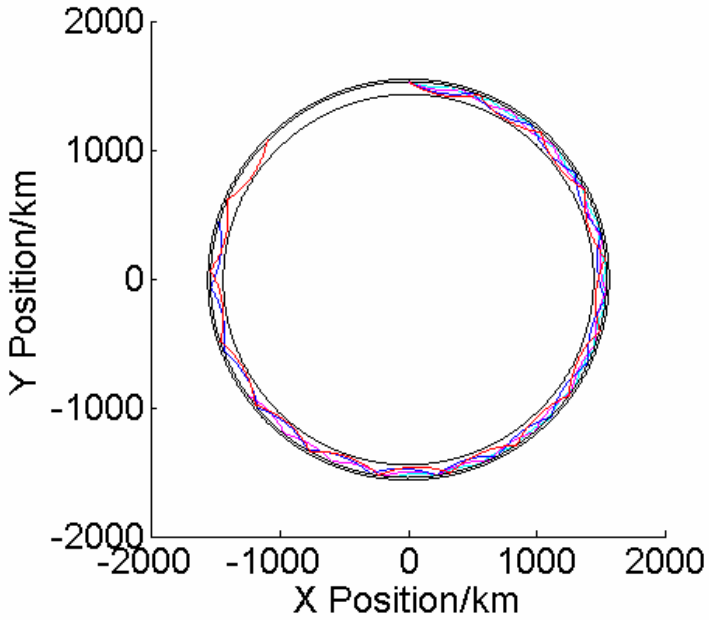

Figure 16. Rays emitted at 20^{o}, 25^{o}, 30^{o}, and 32.5^{o} below the horizontal (shown in cyan, magenta, black, and red, respectively). Each ray has been traced here for 13 reflections.

These calculations illustrate how a co-located source and receiver might be capable of performing a long-distance acoustic propagation experiment on Europa. This could be done by the module emitting a sufficiently strong acoustic signal. Inversion of the received signal could be used to estimate the sound speed profile and general environment of the ocean, and the properties of the seabed. The fidelity of the signal could be inverted to obtain information about the ice (particularly the roughness of the base of the ice pack). The advantage of being able to obtain data from the entire ocean from a single sensor is clear.

In turn, to conserve power, the sensor could operate in passive mode, detecting the ambient sounds in the moon and how they are modified by the environment (the seabed, the ice and the ocean *etc*.), and inverting them for environmental properties. Such ambient sound would not be unexpected given, for example, the gravitational forces to which Europa is subject during its orbit of Jupiter. The use of passive acoustic provides a possible low-power option, such as would for example be required to monitor the change in seismic and ice-cracking activity during a complete orbit. This passive observation technique might also be applied to the analysis of seismoacoustic signals propagating through the ice, silicates and core.

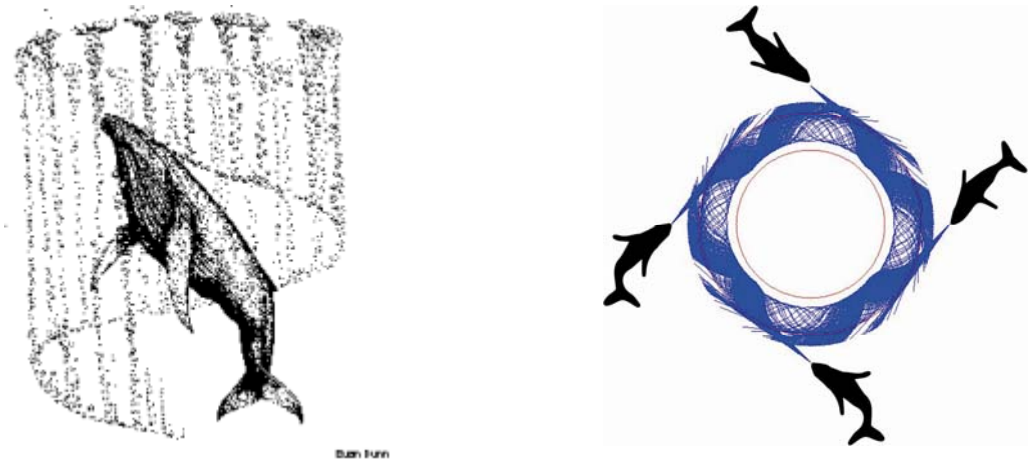

(a) (b)

Figure 17. (a) Humpback whales form bubble nets by diving deep, then swimming in a spiral as they release bubbles from their blowholes. This forms hollow cylinder of bubbles. Prey are trapped in the centre, and the whales then consume them by swimming up through the centre of the net, an activity called 'lunge feeding' (Schematic courtesy of Cetacea.org). (b) Leighton *et al.*[17] proposed that the unique feeding calls emitted by the whales are trapped within the walls of the bubble net.

(a) (b)

Figure 18. Two photographs of spiral bubble nets shown before (a) and during (b) the lunge feeding. (Photographs by Tim Voorheis / www.gulfofmaineproductions.com. Photographs were taken in compliance with United States Federal regulations for aerial marine mammal observation.)

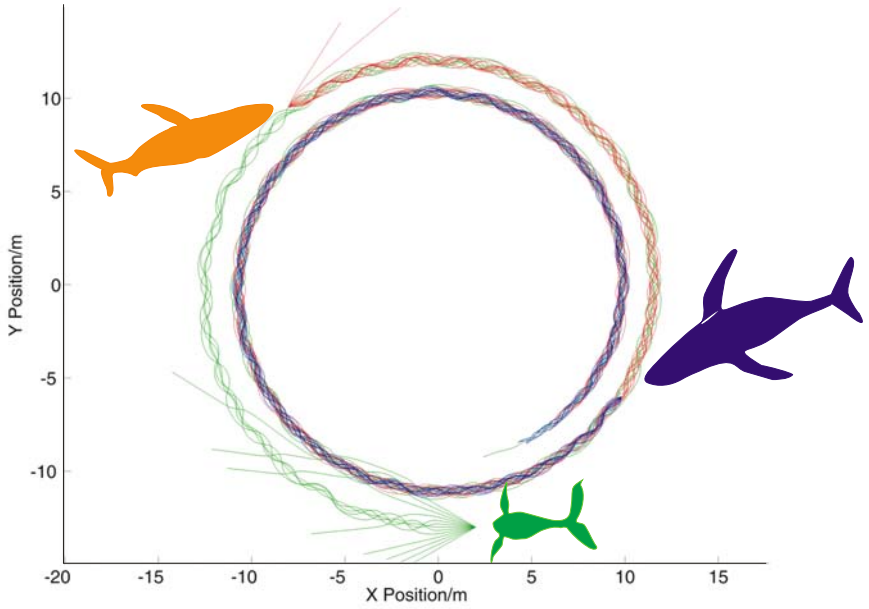

(a)

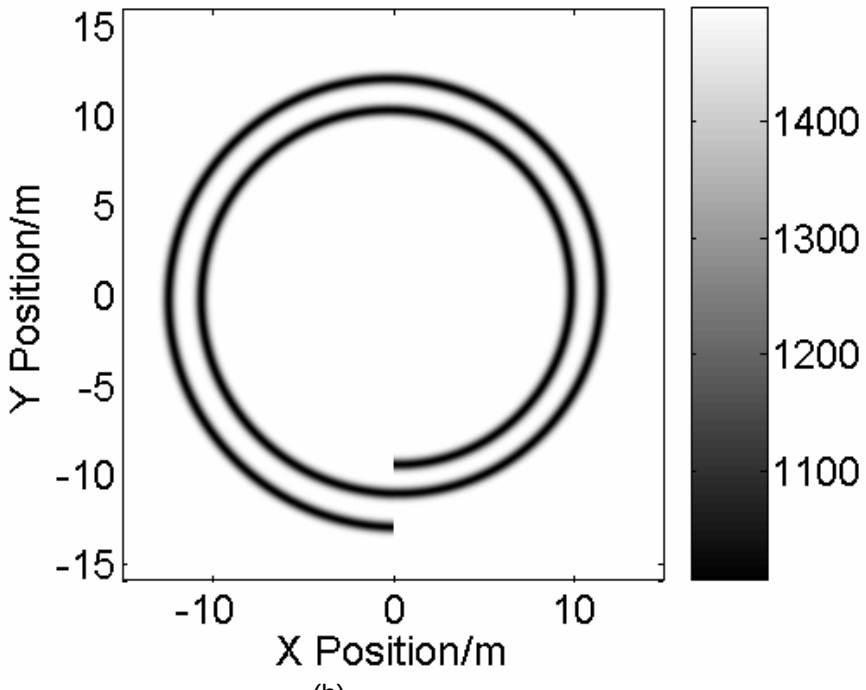

(b)

Figure 19. (a) Ray paths in a spiral bubble net were the bubble population is assumed to create sound speed profiles that can be approximately represented as a Gaussian function falling from 1500ms^{-1} in bubble-free water, to a minimum of 800 ms^{-1} along the centre line of the bubble wall that tracks around the spiral (shown in (b)). Into this net are shown rays emanating from three whales. As discussed in Leighton *et al.*[17], in the absence of information regarding the beam profile and the bubble population, dimensions had to be estimated. Plotting of an individual ray stops if it never enters, or if it leaves the bubble wall. Attenuation of the rays which remain within the wall is taken here to warrant plotting a ray once it has completed a little over one complete circuit, because of loss of signal. Scattering off the boundaries of the net is not included.

As a coda to this investigation, it is interesting to note the similarity between this analysis of Europa and a study in cetacean acoustics. In 2004, Leighton *et al.*[17] proposed that cetacea use bubble nets as acoustics waveguides to create a sonic trap for prey, as shown in Figure 17. Interestingly, Figure 17(b) depicts a circular waveguide, which bears resemblance to the Europan waveguide shown in Figure 16.

It has been known for decades that humpback whales, either singly or in groups, sometimes dive deep and then release bubbles to form the walls of a cylinder, the interior of which is relatively bubble-free (Figure 17). The prey are trapped within this cylinder, for reasons previously unknown, before the whales 'lunge feed' on them from below. An acoustical explanation for why the prey are trapped has been proposed. When the whales form such nets, they emit very loud, 'trumpeting feeding calls', the available recordings containing energy up to at least 4 kHz. A suitable void fraction profile would cause the wall of the cylinder to act as a waveguide.

Data on these bubble nets is understandably scarce, limiting the extent to which their acoustical properties can be predicted. However this paper utilises the Europa models to demonstrate new features into the bubble net research programme. Previous modelling was restricted to circular nets only, as this was the geometry of net of the authors were aware. However since that work[3,17] photographic evidence of spiral nets had come to our attention (Figure 18). The predicted ray paths for the emissions of three whales emitting into a spiral bubble net are shown in Figure 19, for rays which are initially trapped in the bubble layer. A second mechanism, shown in Figure 20 and equally hypothetical, schematically shows rays which propagate within the bubble-free water layers between the bubbly layers of the spiral, reflecting from the interfaces with bubbly water. Since they propagate through bubble-free water in this scenario, such rays should suffer less attenuation than is experienced by rays propagating within the bubbly layer. Of course the ray paths shown in Figures 19 and 20 only tell part of the story: there will be ray paths which propagate at times in the bubble layer, and then leave it to enter the bubble-free layer, of the spiral; reflections at interfaces between bubbly- and bubble-free water will be only partial; and both are restricted by the limitations of ray representation.

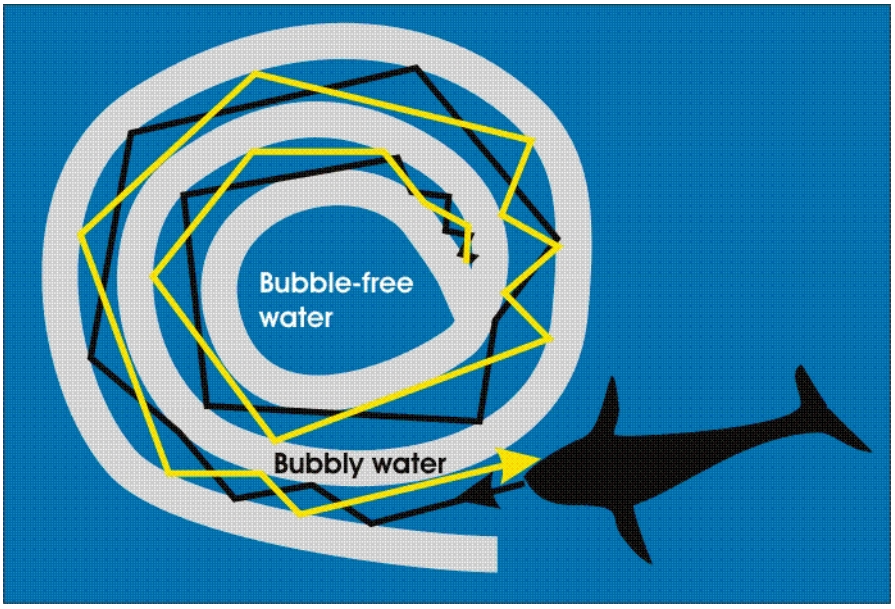

Figure 20. Schematic of ray paths in the bubble-free layer of the spiral. The grey colouration indicates bubbly water, and the blue indicates bubble-free water. A single ray is shown emitted from the whale into the spiral, shown black during its inbound journey and yellow on its outbound path.

However the figures do suggest that, as with the circular bubble net[3,17], the spiral net could be used to form a 'wall of sound', with a quiet centre. If the prey, in the centre of the net, approach the walls they become startled by the intense sound (which may not only be subjectively loud, but also affect a fish

swim bladder). The natural schooling response of prey to startling would, in the bubble net, be transformed from a survival response into one that aids the predator in feeding.

Why some nets should be spiral is not clear. It may be a pragmatic or incidental response to practical limitations, in that maximising the bubble net size may necessitate that whales continue to blow bubbles even as they begin to ascend within the net. Conceivably however the circular and spiral nets may have different properties. Three possible advantages of the spiral configuration are:

- A wall of sound can be generated using acoustic paths which propagate in bubble-free water (Figure 20) and hence suffer less attenuation than seen for acoustic paths in bubbly water (to which circular nets are restricted);

- The spiral net contains more scattering interfaces between 'bubble-free' and bubbly water, such that whilst a ray which leaves the circular net is lost from the net, a ray which refracts out of a region of bubbly water in the spiral net can remain trapped within the spiral system;

- The geometry of Figure 20 shows how the whale could speculatively obtain feedback on the performance of the spiral net, since the efficiency of the "wall of sound" could be diagnosed through monitoring the outbound sound as it leaves the spiral.

4 CONCLUSIONS

This paper has demonstrated two examples for the use of acoustics in space exploration. The sound of 'waterfalls' on Titan was predicted and, using the same approach, the sound of a splashdown was predicted (both sets of recordings being placed on the internet). Comparison between the predictions of several higher-order moments suggests that it is nevertheless possible quantitatively to detect discrepancies between simulated and real sounds, a suggestion confirmed by listening tests of real and simulated terrestrial waterfalls. The use of acoustics in space exploration was then further explored with respect to the propagation of signals in the ice seas of Europa. An analytical approach allowed some preliminary predictions to be made. These were confirmed by two-dimensional numerical modelling which, like the analytical modelling, ignored the curvature of the moon surfaces. The numerical modelling was refined to include the curvature of Europa, and the model then adapted to investigate acoustic propagation in the spiral bubble nets of humpback whales.

Future work on this project will include:

- predictions of the under-ice ray paths for wider beam patterns at source, so that the presence of convergence and shadow zones can be identified;

- incorporation of the sound speed profile in which gravity is a variable (equation (17)).

- demonstrations of how the separate contributions of the individual terms in equation (17) contribute to the departures from linearity in the sound speed profile;

- incorporation of estimations of signal attenuation for long-range propagation in the Europan sea.

Compared to many sensors deployed for space exploration, acoustical systems have many advantages, in terms of bandwidth, power consumption, size and weight. It is important that a fifth advantage does not count against proper utilisation of the methodology: acoustical instrumentation is inexpensive, but that does not mean that acoustics can be seen as a bonus system which can readily be implemented by non-acousticians. Because acoustics has such a wide range of applications, and the equipment can be purchased relatively cheaply, acoustic technology is often bought "off-the-shelf" by experts in other disciplines. From chemistry, to biology, to materials science, this has resulted in many examples of poor science, many of which have gone unrecognised as such by many. Worse than a failure to use acoustics to its full potential, is to use it to produce a trusted answer which is wrong.

ACKNOWLEDGEMENTS

The authors are grateful to Dr S.D. Richards for bringing to their attention the photographs of the spiral form of bubble nets.

REFERENCES

1. N.A.-L. Ghafoor, J.C. Zarnecki, P.G. Challenor and M.A. Srokosz, Wind-Driven Surface Waves On Titan. *J. Geophys. Res.* **105**(E5), 12077-12091. (2000).
2. T.G. Leighton and P.R. White, The sound of Titan: a role for acoustics in space exploration. *Acoustics Bulletin* **29**, 16-23. (2004).
3. T.G. Leighton, From seas to surgeries, from babbling brooks to baby scans: The acoustics of gas bubbles in liquids, *International Journal of Modern Physics B,* **18**(25), 3267-3314. (2004).
4. H. Svedhem, J.-P. Lebreton, J. Zarnecki and B. Hathi, Using Speed of Sound Measurements to Constrain the Huygens Probe Descent Profile. In: Wilson, A. (Ed.), *Proc. Int. Workshop on Planetary Probe Atmospheric Entry and Descent Trajectory Analysis and Science,* Lisbon, 6-9 October 2003. ESA SP-544, pp. 221-228. (2004).
5. T.G. Leighton, BBC News Online, (July 1, 2004).
6. T.G. Leighton and A.J. Walton, An experimental study of the sound emitted from gas bubbles in a liquid, *European Journal of Physics*, **8**, 98-104. (1987).
7. T.G. Leighton, P.R. White, and M.F. Schneider, The detection and dimension of bubble entrainment and comminution, *Journal of the Acoustical Society of America*, **103**(4), 1825-1835. (1998).
8. M.R. Loewen and W.K. Melville, A model for the sound generated by breaking waves. *J. Acoust. Soc. Am.* **90**, 2075-2080. (1991).
9. T.G. Leighton, *Bubble Acoustics from Seas to Surgeries*. Springer Series in Modern Acoustics and Signal Processing series, Springer, 2005 (in preparation).
10. T.G. Leighton, www.isvr.soton.ac.uk/fdag/uaua.htm, 2004.
11. T.G. Leighton, P.R. White, and D.C. Finfer, Possible applications of bubble acoustics in Nature. *Proc. of the 28th Scandinavian Symposium on Physical Acoustics* (Ustaoset, Norway, 2005) (Proceedings available on CD only).
12. J.M. Mendel, Tutorial on higher-order statistics in signal processing and system theory: theoretical results and some applications; *Proc. IEEE*, 79, 278-305 (1991).
13. P.R. White, T.G. Leighton and G.T. Yim, Exploitation of higher order statistics to compute bubble cloud densities; evading Olber's paradox, *Proc. 7th European Conf. on Underwater Acoustics*, 223-228. (2004).
14. P.R. Leung T.S-T. and P.R. White, Robust Estimation of Oceanic Background Noise Spectrum *Proc. 4th IMA Int. Conf. on Mathematics in Signal Processing*, Warwick*, unpaginated*, (1996).
15. T.G. Leighton, S.D. Meers and P.R. White, Propagation through nonlinear time-dependent bubble clouds, and the estimation of bubble populations from measured acoustic characteristics. *Proceedings of the Royal Society A,* **460**(2049), 2521-2550, (2004).
16. H. Medwin, Speed of wound in water for realistic parameters. J. Acoust. Soc. Am. **58**, 1318, (1975).
17. T.G. Leighton,, S.D. Richards S D and P.R. White. Trapped within a 'wall of sound': A possible mechanism for the bubble nets of humpback whales. *Acoustics Bulletin* **29**, 2004, 24-29
18. W.H. Munk, W.C. O'Reilly and J. L. Reid. Australia-Bermuda sound transmission experiment (1960) revisited. *J. Phys. Oceanogr.* **18**, 1876- 1898 (1988).